



Diffuse light field imaging through thick scattering media

HONGKUN CAO,¹ XIN JIN,^{1,2,*}  JUNJIE WEI,^{1,2}  YIHUI FAN,² 
AND DONGYU DU² 

¹*Pengcheng Laboratory, Shenzhen 518055, China*

²*Shenzhen International Graduate School, Tsinghua University, Shenzhen 518055, China*

**jxin.xin@sz.tsinghua.edu.cn*

Abstract: Scattering imaging through thick scattering media is often hindered by extremely low signal-to-noise ratios (SNRs) due to the ballistic-photon signal becomes negligible. To break through the super low SNR limit, we propose a diffuse light field imaging model (DLIM) to retrieve forward-scattered photons as signals. In this model, a diffuse source is constructed in an angular accumulated light field image by synthesizing the radiance sources captured from various view images. After that, the clear image could be solved analytically as a source term based on the diffusion equation by deconvoluting the diffuse Green function, which builds the diffuse light field convolution theorem. To demonstrate the physical process mathematically, we propose three-plane parametrization, which facilitates the derivation of DLIM from radiative transfer in each view image to diffuse approximation in the synthesized light field image. This is the first physically-aware scattering light field imaging model, extending the conventional light field imaging framework from free space into diffuse media. Extensive experiments confirm that the DLIM can reconstruct the target objects even when scattering light field images are reduced to random noise at extremely low SNRs. Compared to state-of-the-art scattering light field imaging methods like plography, the proposed method outperforms by 1.70 dB/4.76 dB peak-signal-noise-ratio (PSNR) and 0.167/0.172 structural-similarity-index-measure (SSIM) higher, on average, for passive-luminous/self-luminous targets, respectively.

© 2025 Optica Publishing Group under the terms of the [Optica Open Access Publishing Agreement](#)

1. Introduction

Imaging through disordered media is hampered by random scattering events of photons, which has been a long-standing challenge for optical imaging. Scattering imaging under natural light is beneficial to many fields, such as auto-driving, underwater exploration, aviation safety, and so on. Unfortunately, imaging through highly scattering media is challenging because the propagation paths for most of the light are randomly disturbed and become scattering light, resulting in noise in the image, only slight ballistic photons produce signal. The scattering light consists of forward scattering photons reflected by object and backward scattering photons that are only reflected and refracted by scattering media. Jaffe-McGlamery (J-M) physically model above light components for simulation of underwater imaging [1,2]. By ignoring forward scattering photons, the J-M model can be simplified as only including direct light and atmosphere light [3–6]. Based on the simplified J-M model, various dehazing methods have been proposed, which aims to remove scattering noise in image and improve the SNR of reconstructed images [3–20]. However, the imaging capability is limited at weak scattering area, which is because the effective signal provided only by ballistic photons drops off as scattering becomes stronger, causing super low SNR. Thus, the utilization of scattering photon as signal becomes critical for SNR gain. Imaging methods have been proposed for microscopic imaging with utilization of scattering photons by exploiting speckle correlation [21,22], transmittance matrix [23,24], phase conjugation [25,26], and wavefront shaping [27,28], etc. Although imaging through extremely thick scattering media (several tens of optical thicknesses) is possible, they are limited to the coherent light source and

microscale of the target, which are hardly applicable in imaging large targets under natural light. Therefore, imaging large targets in strongly scattering media under natural light is challenging.

Light field imaging methods capture lights from multiple views with more ballistic photon collection and noise suppression, which can improve imaging capability through scattering media with higher SNR [29–37]. For instance, light field imaging methods aim to distinguish ballistic photons from scattering photons by using the intensity consistency of ballistic photons in all perspective images [29,30] and extract ballistic photons by assuming the Gaussian distribution of scattering photons [31]. Moreover, the depth extraction of the light field using the J-M model resolves the target information [32]. Peplography models scattering photons with statistical estimation and extract the ballistic photons based on the photon counting model under an integral imaging framework [33]. However, those methods rely on ballistic photon imaging and scattering noise reduction, which limits the penetrated optical thickness.

Here, a physically-aware imaging model is derived leveraging the light field framework based on radiate transfer theory, which is called diffuse light field imaging model (DLIM). Beyond ballistic photon signal, it can convert the forward scattering photons into signal by solving diffusion equation (DE). After that, the clear image could be solved analytically as a source term based on the diffusion equation by deconvoluting diffuse Green function, which builds the diffuse light field convolution theorem. To demonstrate the physical process mathematically, we propose three-plane parametrization, which facilitates the derivation of DLIM from radiative transfer in each view image to diffuse approximation in the synthesized light field image. Finally, the object image can be reconstructed from the refocused scattering light field image using the diffuse kernel with computational complexity $O(N^2 \log N)$ for $N \times N$ image resolution. In addition, the backscattering photons (atmosphere light) still can be removed with some dehaze algorithms. Compared with state-of-the-art scattering light field imaging method Peplography [30], the proposed DLIM outperforms Peplography by 1.70 dB/4.76 dB Peak-Signal-Noise-Ratio (PSNR) and 0.167/0.172 Structural-Similarity-Index-Measure (SSIM) higher, on average, for passive-luminous/self-luminous targets, respectively. Well-known dehaze methods including image enhancement and prior-based methods are mostly ineffective in experiments when addressing these highly scattered images.

2. Proposed diffuse light field imaging model

As shown in Fig. 1(a), in a linear light field imaging system, a quasi-point of impulse response can be observed in the imaging plane for a conventional imaging system, and the images can be represented by the convolution between light source distribution and point spread function (PSF) as follows:

$$L(u, v, s, t) = L_O(u, v, \xi, \eta) \otimes h_I(u, v, s, t), \quad (1)$$

where $L(u, v, s, t)$ is the light field images, $L_O(u, v, \xi, \eta)$ and $h_I(u, v, s, t)$ represent the distribution of the light source and the point spread function (PSF) of imaging system, respectively.

In a scattering light field imaging, the ballistic photons can penetrate scattering media as depicted by blue points, while the other two types of scattering photons are randomly distributed in the imaging plane as depicted by red and green points as shown in Fig. 1(b). As a result, the impulse response, in other words, the PSF of scattering light field becomes speckle patterns, in which tiny highlights of intensities in images near ballistic-photon accumulated positions can be observed as seen in Fig. 1(c). Here we assume another convolution term as scattering impulse denoted by $h_S(u, v, s, t)$ to be introduced into the imaging process as defined in Eq. (2), as depicted by Fig. 1(d).

$$L(u, v, s, t) = L_O(u, v, \xi, \eta) \otimes h_I(u, v, s, t) \otimes h_S(u, v, s, t) \quad (2)$$

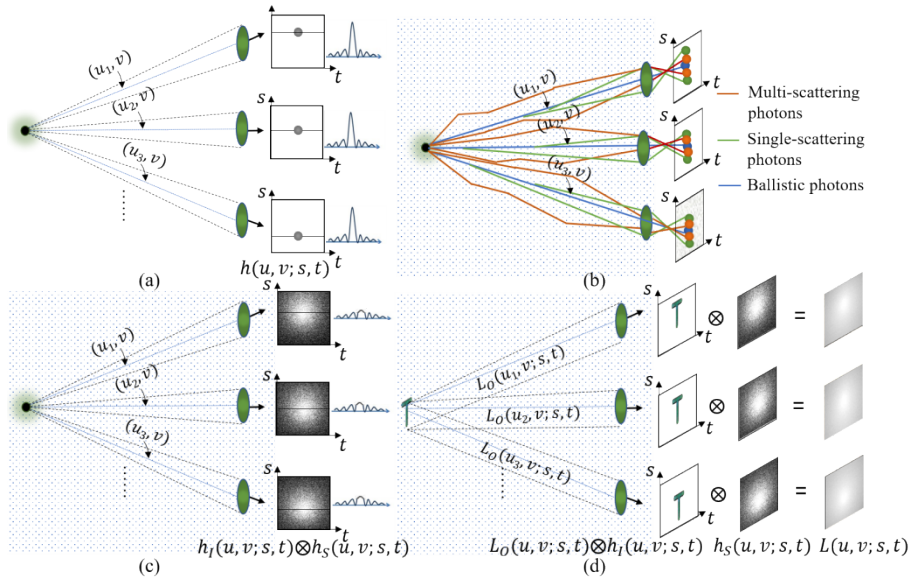


Fig. 1. The construction principle of light field imaging in scattering media. (a) The PSF of conventional light field imaging without considering scattering effect. (b) The scattering light field images consist of various scattering photons. (c) The PSF of scattering light field images. (d) The scattering light field imaging framework that is represented by the convolution between the object image and scattering PSF.

2.1. Three-plane parameterization

To derive the convolution kernel $h_s(u, v, s, t)$ of scattering light field imaging model conveniently, a three-plane coordinate representation is proposed. The conventional two-plane parameterization of light field only add another angular dimension to spatial dimension in imaging space to record the emitting direction of light from object. This is under the condition that the direction of $\mathbf{u}(u, v) \rightarrow \mathbf{s}(s, t)$ is equal to the emitting direction of light from object to camera, since only line transport of light is involved. However, in the diffuse light-field framework, the direction of $\mathbf{u}(u, v) \rightarrow \mathbf{s}(s, t)$ is not equal to the emitting direction of light from object to camera, since not only ballistic but also scattering photons came into \mathbf{u} -plane and received by \mathbf{s} -plane. Yet it is critical to model both ballistic and scattering photon in our modeling process. Thus, how to describe the radiance in spatial and angular dimensions of both ballistic and scattering photons under light field framework is vital to clearly unfold the mechanism of scattering light field imaging. In the proposed three-plane parameterization, to separately describe the ballistic and scattering photons, we add another plane $\xi = (\xi, \eta)$ in object space and using the two-plane coordinates of $\xi - \mathbf{u}$ to specifically describe the radiance of ballistic photons, such as $L(\xi, u)$, since those line-transported photons from object plane ξ to camera plane \mathbf{u} must be ballistic photons. The radiance of scattering photon are represented as $L(u, s)$ using another two-plane of $\mathbf{u} - \mathbf{s}$. As seen in Fig. 2(a), for simplicity, only one dimension for each plane is considered for each plane and all derivations are appropriate for the two-dimensional plane cases. For example, the radiance of the object point ξ_0 towards u_1 is denoted as $L(\overrightarrow{\xi_0 u_1})$, and the radiance received in pixel s_1 coming from u_1 is denoted as $L(\overrightarrow{u_1 s_1})$. Noting that the $L(\overrightarrow{\xi_0 u_1})$ is only ballistic photon, whereas the $L(\overrightarrow{u_1 s_1})$ could be ballistic, scattering photons or mix of them. In particular, we add another auxiliary plane, the k -plane between object plane and camera plane to describe the radiance of incident scattering photons came to camera plane for constructing radiative transfer

function as seen in Fig. 2(b). Then the key component is how to construct the relation of radiance for those ballistic photons, scattering photons under light field framework with above three-plane parameterization, which will be demonstrated in next section.

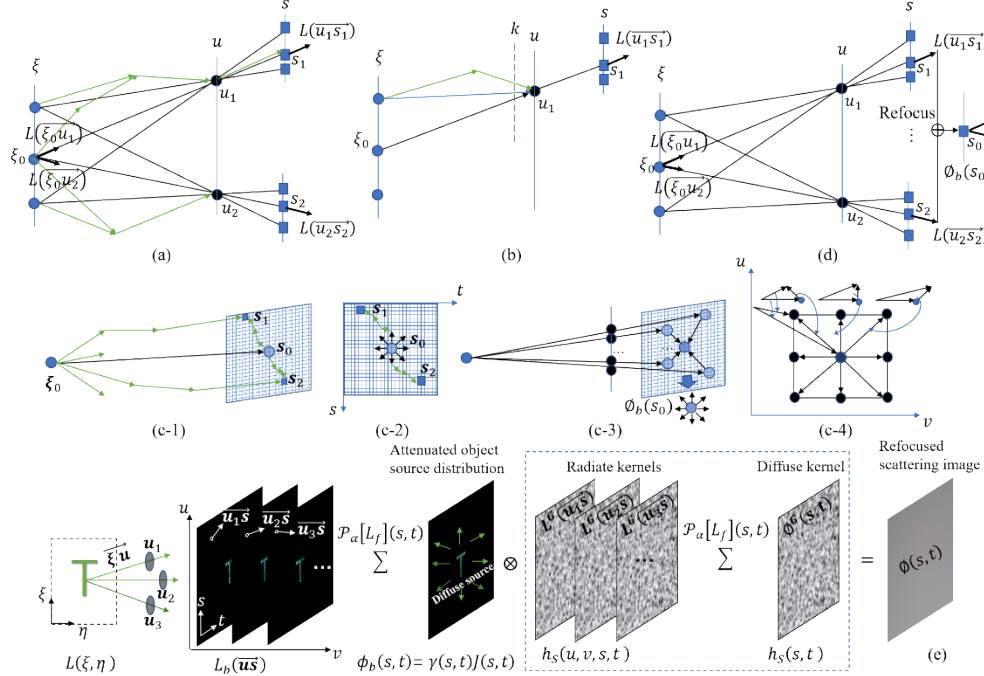


Fig. 2. The schematic illustration of physical process for diffuse light field imaging. (a) Analysis of radiance distribution in light field images considering both scattering and ballistic photons. (b) Example of radiance $L(\vec{u}_1 \vec{s}_1)$ contributed by ballistic and scattering photons. (c) The explanation of diffusion approximation for radiate light field imaging. (c-1) The light source radiate photons consist of ballistic and scattering photons into image plane, where the photons in s_1, s_2 can be regarded as radiated from the radiate source s_0 . (c-2) the diffuse source s_0 must be a concentric source radiating photons towards various directions. (c-3) Construction process of diffuse source in angular accumulated light field image containing ballistic photons from various directions. (c-4) The projection explanation that ballistic photon captured from various views contribute to a concentric diffuse source in angular accumulated light field image. (d) General schematic of diffuse source $\Phi_b(s)$ leveraging light field imaging framework. (e) Forward framework of diffuse light field imaging modeling (DLIM).

2.2. Radiative light field imaging model

Radiative light field model refers to analyzing the radiance distribution in scattering light field images with three-plane parameterization. Here we take only one of light field perspective u_1 as an example. The received radiance is contributed by two terms composed of ballistic photons and scattering photons as defined by

$$L(\vec{u}_1 \vec{s}) = L_b(\vec{u}_1 \vec{s}) + L_s(\vec{u}_1 \vec{s}), \quad (3)$$

where $L_b(\vec{u}_1 \vec{s})$ indicates the ballistic term and $L_s(\vec{u}_1 \vec{s})$ means the scattering term as depicted by black and green line in Fig. 2(a) [35]. Here the ballistic photons are attenuated as the distance

between camera and object increases, as defined by

$$L_b(\vec{u}_1\vec{s}) = L(\vec{\xi}\vec{u}_1)\exp(-\mu_s|\vec{\xi}\vec{u}_1|), \quad (4)$$

where the $\mu_{eff} = \mu_a + \mu_s'$ is the effective attenuation coefficient, and μ_a and μ_s' are the absorption and reduced scattering coefficients [35]. The scattering photons $L_s(\vec{u}_1\vec{s})$ consists of single and multiple scattering photons as depicted by blue and green lines between $\vec{\xi}$ and \vec{u} planes in Fig. 2(b), can be mathematically described as

$$L_s(\vec{u}_1\vec{s}) = \mu_s \int L(\vec{k}\vec{u}_1)p(\vec{k}\vec{u}_1, \vec{u}_1\vec{s})dk, \quad (5)$$

where k means the coordinate in the auxiliary plane before camera plane as seen in Fig. 2(b) and $p(\vec{k}\vec{u}_1, \vec{u}_1\vec{s})$ is the phase function. Thus, based on energy conservation, a partial differential equation can be constructed as

$$\vec{u}\vec{s} \cdot \nabla L(\vec{u}\vec{s}) + \mu_{eff}L(\vec{u}\vec{s}) = L_b(\vec{u}\vec{s}) + L_s(\vec{u}\vec{s}). \quad (6)$$

It is revealed that the received scattering radiances distribution $L(\vec{u}\vec{s})$ is correlated to the object radiance through attenuated source term $L_b(\vec{u}\vec{s})$ according to above radiate transfer equation (RTE), since $L_b(\vec{u}\vec{s})$ is linearly attenuation version of the object radiance $L(\vec{\xi}\vec{u})$ according to Eq. (4). Thus, if the source term $L_b(\vec{u}\vec{s})$ can be reconstructed from scattering term $L(\vec{u}\vec{s})$, the object radiance will be obtained as a result. To solve above equation, the Green function can be introduced. Let's assuming an impulse object source, such as $\delta(|\vec{\xi}\vec{u}| - |\vec{\xi}_0\vec{u}|)$, then $L_b^\delta(\vec{u}\vec{s}) = L(\delta(|\vec{\xi}\vec{u}| - |\vec{\xi}_0\vec{u}|))\exp(-\mu_s|\vec{\xi}_0\vec{u}|)$. Let $L_b(\vec{u}\vec{s}) = L_b^\delta(\vec{u}\vec{s})$ in Eq. (6), the solution is an impulse response of this system, which is called Green function and denoted as $L^G(\vec{u}\vec{s})$. Then the radiance distribution in imaging plane of perspective u can be modeled as convolution between ballistic radiance distribution $L_b(\vec{u}\vec{s})$ and Green function $L^G(\vec{u}\vec{s})$ as

$$L(\vec{u}\vec{s}) = L_b(\vec{u}\vec{s}) \otimes L^G(\vec{u}\vec{s}) \quad (7)$$

The Green function can be solved by expanding radiance with spherical harmonics, an infinite approximation to RTE is obtained. The P_N approximation means taking the first N spherical harmonics, which gives $(N + 1)^2$ coupled partial differential equations. Diffusion approximation as the P^1 approximation to RTE has wide usage in biological imaging [38–40]. When imaging distance larger than ℓ_t that is transport mean free path and the media is isotropic, the radiate transfer is well described by diffusion equation [41,42].

2.3. Diffusion approximation of radiative light field imaging model

Leveraging the light field imaging framework, we can capture discrete radiances $L(\vec{u}\vec{s})$, if we accumulate various angular light field images, the accumulated light field can be approximated as

$$\int L(\vec{u}\vec{s})du = \int L_b(\vec{u}\vec{s}) \otimes L^G(\vec{u}\vec{s})du. \quad (8)$$

It means the angular accumulated scattering light field image can be composed as superposition of all perspective scattering images resulted by one clear image, such as $L_b(\vec{u}\vec{s})$ convoluting one radiate impulse function, such as $L^G(\vec{u}\vec{s})$. To obtain the analytic solution of target signal L_b , assuming the homogeneous and isotropic scattering media, the Eq. (8) is transformed into

$$\int L(\vec{u}\vec{s})du = \int L_b(\vec{u}\vec{s})du \otimes \int L^G(\vec{u}\vec{s})du. \quad (9)$$

The last term is noted as $\emptyset^G(s) = \int L^G(\vec{u}\vec{s})du$, which becomes into the impulse function of fluence rate in diffuse system [35,38], which can be solved from diffuse equation as defined in

Eq. (10),

$$D\nabla^2\theta(s) - \mu_a\theta(s) = \theta_b(s), \quad (10)$$

where D is the diffuse coefficient $1/(3^*(\mu_a + \mu_s(1 - g)))$, g is the isotropic coefficient [35]. We can use the Neumann boundary ($\frac{\partial\theta}{\partial r} = 0$) to solve Eq. (8) [38,39]. The mathematical procedure for solving DE can be found in any literature refer radiate transfer. Here we give the result directly, which is defined as

$$\theta^G(s) = \frac{1}{2\sqrt{\mu_a D}} \left(e^{-\sqrt{\frac{\mu_a}{D}}|s-s_0|} + e^{-\sqrt{\frac{\mu_a}{D}}|s+s_0|} \right) \quad (11)$$

Noting that a diffuse sourced term is constructed by accumulating angular perspective light field images, specifically $\theta_b(s) = \int L_b(\vec{u}s)du = \gamma \int L(\vec{\xi}u)du$, where $\gamma = \exp(-\mu_s|\vec{\xi}u|)$ is the Lambert-Beer attenuation ratio. Simply, the diffuse source can be defined as $\theta_b(s) = \theta(\xi)\gamma(s)$, where coordinates ξ and s have been matched by imaging system and $\gamma(s) = \exp(-\mu_s z(s))$.

The physical process is demonstrated as seen in Fig. 2(c). Assuming a point light source at ξ_0 , it radiates photons to various directions and the scattered photons reach pixels of imaging plane randomly, such as $s_1 = [s_1, t_1; z+f]$, $s_2 = [s_2, t_2; z+f]$, where f is focusing length of imaging lens. As seen in Fig. 2(c-1), the photon diffuse route from source to sensor pixel ($\xi_0 \rightarrow s_1$), $\xi_0 = [\xi_0, \eta_0; 0]$, could be approximated by two parts containing line transport of ballistic photon ($\xi_0 \rightarrow s_0$), $s_0 = [s_0, t_0; z]$, and the diffusion process in imaging plane ($s_0 \rightarrow s_1$), same as other pixels, such as s_2 . This is enabled under a precondition that a diffuse source exists in imaging plane, which allows all pixels in imaging plane can be diffused by this source as seen in Fig. 2(c-2). In the light-field approximation model, the diffuse source is formed by accumulating radiance coming from various directional ballistic photons of object source leveraging multi-view capturing. That is, taking advantage of light field imaging framework, all directional object radiance will be integrated by refocus and then a diffuse source $\theta_b(s_0)$ is constructed in synthesized light field image as an attenuated radiance source as seen in Fig. 2(c-3), as a result the whole angular accumulated light field image can be the diffuse result of this source term. More specifically, assuming a grid of capture spots as shown in Fig. 2(c-4), each projection of the lines of ballistic photon transport from the object source to each view will contribute one concentric radiance to the diffuse source in the angular accumulated light field image.

For instance, an object point source ξ_0 radiates photons towards various directional, such as $\vec{\xi}_0 u_1$ and $\vec{\xi}_0 u_2$, will be integrated as diffuse source at pixel s_0 of angular accumulated light field image with attenuated energy as seen in Fig. 2(d).

In the original light field imaging equation of Eq.(2), $h_I(u, v, s, t) \otimes h_S(u, v, s, t)$ can be combined as radiate kernel $h_{IS}(u, v, s, t)$, which can be obtained by setting the radiate Green function $L^G(\mathbf{u} \rightarrow \mathbf{s})$, $\mathbf{u} = [u, v; z]$, $\mathbf{s} = [s, t; z+f]$ as $h_{IS}(u, v, s, t)$ assuming $h_I(u, v, s, t)$ is an idea impulse response. According to the theorem of filtered light field photography, the 4-D convolution of light field can be simplified as 2-D convolution, as defined

$$\mathcal{P}_\alpha \circ C_{\mathcal{K}}^4 \equiv C_{\mathcal{P}_\alpha[\mathcal{K}]}^2 \circ \mathcal{P}_\alpha \quad (12)$$

where \mathcal{P}_α is the refocus operator defined as

$$\mathcal{P}_\alpha[L_f](s, t) = \frac{1}{\alpha^2 f^2} \iint L_f \left(u \left(1 - \frac{1}{\alpha} \right) + \frac{s}{\alpha}, v \left(1 - \frac{1}{\alpha} \right) + \frac{t}{\alpha}, u, v \right) dudv, \quad (13)$$

where $\alpha = \frac{f}{f+z}$. The $C_{\mathcal{K}}^N$ is an N -dimensional convolution operator with filter kernel \mathcal{K} [43]. Based on the convolution theorem of light field, with the derived diffusion light field imaging model, this theorem can be extended into scattering light field as diffuse light field convolution

theorem by setting the integral of 4D filter kernel as a diffuse kernel, i.e.,

$$\mathcal{P}_\alpha[\mathcal{K}] = \mathcal{O}^G(s) = \mathcal{P}_\alpha[L^G(\mathbf{u} \rightarrow s)]. \quad (14)$$

The above forward process is illustrated heuristically by the diagram in Fig. 2(e). The radiances of an object with the source distribution $L(\xi, \eta)$ are received by the sensors through different lenses at $(\mathbf{u}_1, \mathbf{u}_2, \mathbf{u}_3, \dots)$. The received radiance are represented as radiate source convolving radiate kernel ($L_b(\mathbf{u} \rightarrow s) \otimes L^G(\mathbf{u} \rightarrow s)$). Leveraging theorem of filtered light field photography, we can refocus $L_b(\mathbf{u} \rightarrow s)$ and $L^G(\mathbf{u} \rightarrow s)$ separately, so that a diffuse source $\phi_b(s, t) = \gamma(s, t)J(s, t)$ and diffuse kernel $\mathcal{O}^G(s, t)$ can be obtained. By the way, $J(s, t)$ can be clear image of the object source without scattering. Finally, the refocused scattering light field image $\mathcal{O}(s, t)$ can be represented as an implicit object source distribution $\phi_b(s, t)$ convolving the diffuse kernel $\mathcal{O}^G(s, t)$, the clear image $J(s, t)$ is equal to $\phi_b(s, t)$ dividing $\gamma(s, t)$.

Backward-scattering modeling is required for imaging in dealing with nature scattering environment, in which the back scattering photons without reaching object are involved as strong noise.

Here, we combine the proposed DLIM and simplified J-M model to account for forward scattering lights, backscattering lights, ballistic lights, and light source distribution under light field imaging framework as defined by

$$J^*(s, t) = \phi_b(s, t) \otimes (\mathcal{O}^G(s, t) + 1) + B_\infty(1 - \gamma(s, t)) \quad (15)$$

where $J^*(s, t)$ is the refocused scattering light field image, $\phi_b(s, t) = \gamma(s, t)J(s, t)$ is the distribution of attenuated object source, $J(s, t)$ is the refocused clear light field image, the ballistic attenuation ratio $\gamma(s, t)$ is the same as the medium transmission in J-M model and B_∞ indicates the atmosphere lights, respectively. Here the wavelength is not discussed in whole model derivation, although it is also correlated with the scattering effect, but is out of the scope of this research.

The recovery from the scattering image $J^*(s, t)$ to original image $J(s, t)$ is an inversion procedure of DLIM, which is accomplished by deconvolution using diffuse kernel $\mathcal{O}^G(s, t)$. A closed-form solution exists using the Wiener deconvolution filter:

$$\hat{\mathbf{J}} = \mathbf{F}^{-1} \circ \left[\frac{\mathbf{\Phi}^G}{|\mathbf{\Phi}^G|^2 + \frac{1}{\zeta}} \right] \circ \mathbf{F} \circ \mathbf{J}^*. \quad (16)$$

where \mathbf{F} denotes the discrete Fourier transform matrix, $\mathbf{\Phi}^G$ is the diagonal matrix whose elements correspond to the Fourier coefficients of the diffuse kernel $\mathbf{\Phi}^G$, ζ is a parameter that varies depending on the signal-to-noise ratio at each frequency, and $\hat{\mathbf{J}}$ is estimated original image. The computational complexity of the above equation is only $O(N^2 \log N)$ for $N \times N$ image resolution. Noting that the self-luminous object will not require modeling backscattering photons. For example, various LED panels for advertisement at night, vehicle lights, diffuse optical tomography (DOT) in biological imaging, optical fiber imaging, e.g., whose scattering images are contributed only by forward scattering and ballistic photons. Notably, the optical thickness can be estimated using visibility multiplying $|\log 0.05|$, which can be measured with a Nephelometer for fog environments [44]. Then the scattering coefficient can be evaluated from optical thickness and depth that can be obtained with laser distance meter for outdoor environments. The exponential of optical thickness can be regarded as attenuation ratio.

In the case of inversion procedure of backward scattering modeling, the Dark Channel Prior (DCP) as one of well-known J-M based algorithm is used to estimate the transmittance considering atmosphere light [5]. Then the recovered image by DCP will mainly contain forward scattering photons, which can be further reconstructed by using DLIM, which provides further signal from forward scattering photons.

3. Experiments and results

To verify the effectiveness and demonstrate the imaging capability of the proposed DLIM, the imaging experiments for both self-luminous and passive-luminous objects through dense fog under light field imaging framework have been conducted. The self-luminous experiments aim to confirm the reconstruction capability of DLIM by utilizing forward scattering photons, whereas the passive-luminous experiments aim to confirm its effectiveness with strong noise caused by back scattered photons. The experimental scheme is shown in Fig. 3(a), in which different angles of light emitted from the target object are captured by cameras from different views, which are synthesized into the final fluence rate image with the refocus operation. Moreover, in terms of several critical factors effecting diffuse light field modeling, the simulation experiments using physical-based rendering platform have also been carried out to accurately control the relative coefficient values and the experimental results are carefully analyzed.

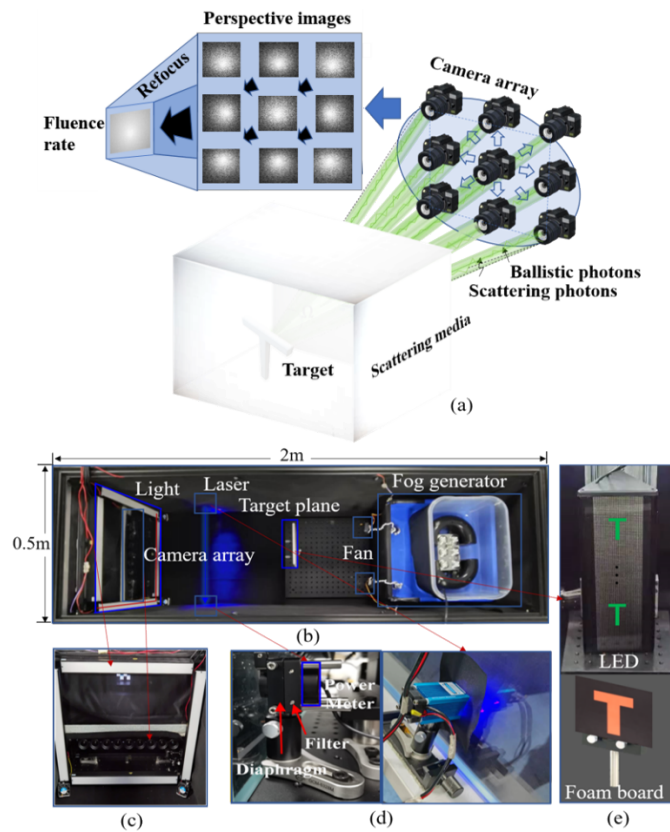


Fig. 3. The diagram of experimental system. (a) Experimental schematic of scattering light field imaging. (b) The experimental set-up. (c) Light and camera system. (d) The measurement system of optical thickness of scattering media. (e) The targets contain self-luminous LED light panel and passive-luminous target of printed foam board.

3.1. Execution of a comprehensive experimental setup

In practical experiments, the targets emerge into volumetric scattering media that is built by a fog chamber, and the cameras are placed behind the chamber in discrete capture positions. When calibrating the light field imaging system, the homography for each perspective is estimated by capturing checkboard images without filling the fog according to Zhang's method [45].

As shown in Fig. 3(b), the fog chamber mainly consists of an ultrasonic fog generator, a light and camera system, a measurement system of optical thickness, and the targets. The camera system is mounted outside the fog chamber. It consists of 9 cameras in a row and all cameras are connected to a synchronous signal generator to ensure the synchronous triggering (see Fig. 3(c)). Each camera consists of a 4 mm lens and a CCD (Flir BFS-PGE-16S2; pixel size, $3.45 \mu\text{m} \times 3.45 \mu\text{m}$; resolution, 1440×1080). The illumination consists of four independent strip light sources (BRD36030), which are set for experiments of passive-luminous light field imaging, and switched off for experiments of self-luminous light field imaging. The system for measuring the optical thickness of scattering media consists of a laser with a wavelength of 480 nm , a power meter, a filter and apertures, as shown in Fig. 3(d). Among them, the filter and diaphragms are to filter out scattering photons and only ballistic photons can be collected by the power meter to make the measurement more accurate. The optical thickness can be defined as $T = \log\left(\frac{P_o}{P_a}\right)$, where P_o and P_a are the original laser power without scattering and the attenuated laser power by the scattering effect of fog, respectively [44]. To test the imaging capacity of the proposed methods, four group of self-luminous and three passive-luminous light field images were acquired through dense fog. The targets for self- and passive- luminous images are shown in Fig. 3(e). The self-luminous targets are the capital letters 'T', 'H', 'U' and a number '2' displayed on the LED panel with an upward motion, and the acquisition frequency is set to same as the motion frequency of letters. The self-luminous light field images contain a total of 8 horizontal and 16 vertical perspectives. The passive-luminous light field images consist of only 9 horizontal perspectives, which allows the image to be captured in a single step. The optical thicknesses for self- and passive- luminous experiments are measured as approximately $OT = 10$ and 9 respectively. Explicitly, the thickness of fog is 0.7 m which is measured from the target to the front of the camera lens. For the optical thickness measurement system, the distance from the laser source to the power meter is 0.5 m . The original value of the power meter is 0.339 W , and the corresponding value for capturing after filling with fog is $5.63 \times 10^{-4} \text{ W}$, so $T = 6.4$ correspondingly. Considering that the distance ratio between the target object and the camera compared with the one between the laser and the power meter is about 1.4, the final optical thickness is about 9. For self-luminous objects, the distance between the target object and the camera lens is about 0.8 m , which means that the distance ratio becomes about 1.6, so the OT equals $6.4 \times 1.6 \approx 10$. Even in artificial experimental environments such as a fog chamber, the optical thickness measurement is not accurate due to the fluctuations of the fog density during image acquisition. The exposure time is set as around 33 ms .

3.2. Verification of DLIM for self-luminous and passive-luminous objects through dense fog

To verify the scattering imaging capacity of the proposed DLIM, 4 group experiments were performed for different self-luminous targets 'T', 'H', 'U' and '2' with different colors and intensities (see (a)-(d) in Fig. 4). As seen in Fig. 4, the first column refers to self-luminous target images for the capital letters 'T', 'H', 'U' and the digit '2' as ground truth (GT). The second column shows one of the perspective images of scattering light field images that were normalized, and the third column shows the scattering light field images synthesized from 8horizontal \times 16vertical perspective images. And the fourth column shows the reconstructed results of scattering light field images for each target by using the proposed DLIM method. Note that the density of fog is hard to be controlled to be stable and consistent during capturing for each target, which will cause fluctuation of real optical thickness for different targets. From the captured perspective images, the differences of real scattering strength for different targets can be recognized, even if all scattering images for the targets are captured aiming at identical scattering conditions with the same optical thickness. The curves of intensity in one row of image are shown in (e)-(h) of Fig. 4. It is obvious that the single perspective image for all targets has a very small dynamic range, from which any target information is impossibly recovered. The

curves of refocused light field images are all Gaussian converged, which is also consistent with our derived diffuse approximation. This shows that the diffuse source is indeed constructed in the refocused image and the whole image is the result of source diffusion. The targets ‘U’ and ‘2’ have higher intensity compared with ‘T’ and ‘H’, which aims to verify that if the improved intensity of the light source can enhance reconstruction quality. As seen in (c), (d) and (g), (h) of Fig. 4, the dynamic ranges of intensity-improved perspective images are further shrunk, and a smoother curve is observed for the light field images, but the reconstruction quality of DLIM is not improved. This reveals that the slightly higher intensity of the light sources cannot improve the reconstruction quality of DLIM. This differs from ballistic-photon-based methods, whose imaging quality is directly correlated with the intensity of light source. All targets are successfully reconstructed from the scattering light field images using the proposed DLIM method. In contrast, the targets are impossibly resolved from refocused light field images directly, even though the speckle noise suppressed and ballistic photons have been accumulated.

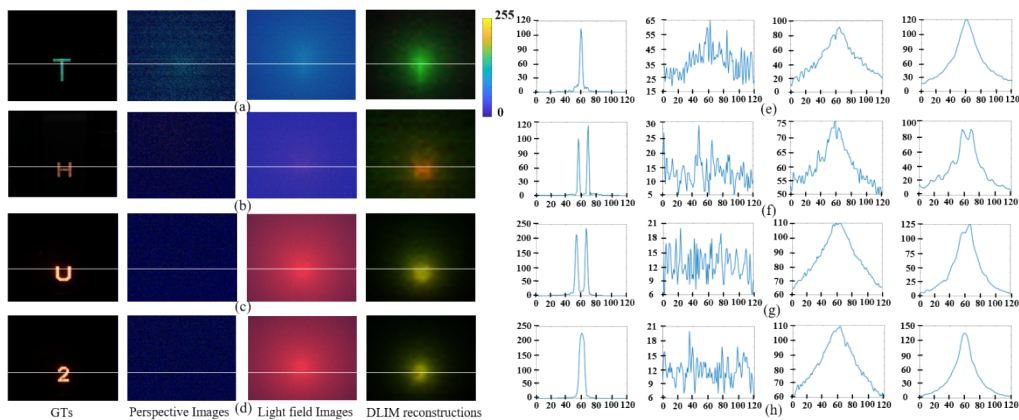


Fig. 4. Experimental results of verification for self-luminous targets by using DLIM. The 1st column refers to self-luminous target images. The scattering images for each target are shown in 2nd column. The light field images are shown in 3rd column. The DLIM-reconstructed results of scattering light field images are shown in 4th column. Images for self-luminous targets of ‘T’, ‘H’, ‘U’, ‘2’ are shown in (a)-(d), and the curves corresponding to one intensity line of left images are shown in (e)-(h), respectively.

The ground truth image is shown in Fig. 5(a), the single perspective scattering image is shown in Fig. 5(b), and the refocused scattering light field image is shown in Fig. 5(c). The optical point spread functions (PSFs) retrieved from single perspective scattering image with ground truth image is shown in Fig. 5(d), whereas the PSF retrieved from refocused scattering light field image with ground truth image is shown in Fig. 5(e). The calculated diffuse kernel PSF is shown in Fig. 5(f). The corresponding frequency spectrum of Fig. 5(d), (e) and (f) are shown in Fig. 5(g), (h) and (i), respectively. Noting that a dominant low frequency component representing ballistic photons is informed in light-field PSF and non-informed in single perspective PSF, but it exists in the frequency spectrum of calculated diffuse kernel PSF. This is the intrinsic principle that the scattering light field image satisfy the diffuse equation, since the low frequency components construct a ballistic-photon caused diffuse source with light field imaging framework. The reconstructed images from single perspective scattering image and refocused scattering light field image with corresponding ground-truth-retrieved PSFs are identical, as seen in Fig. 5(j). However, with the calculated diffuse kernel PSF, they have completely different reconstruct results. The reconstructed image from single perspective scattering image with diffuse kernel is shown in Fig. 5(k), whereas the reconstructed image from refocused scattering light field image

is shown in Fig. 5(l), which confirms the effectiveness of calculated diffuse kernel to scattering light field image and the ineffectiveness to single scattering perspective image.

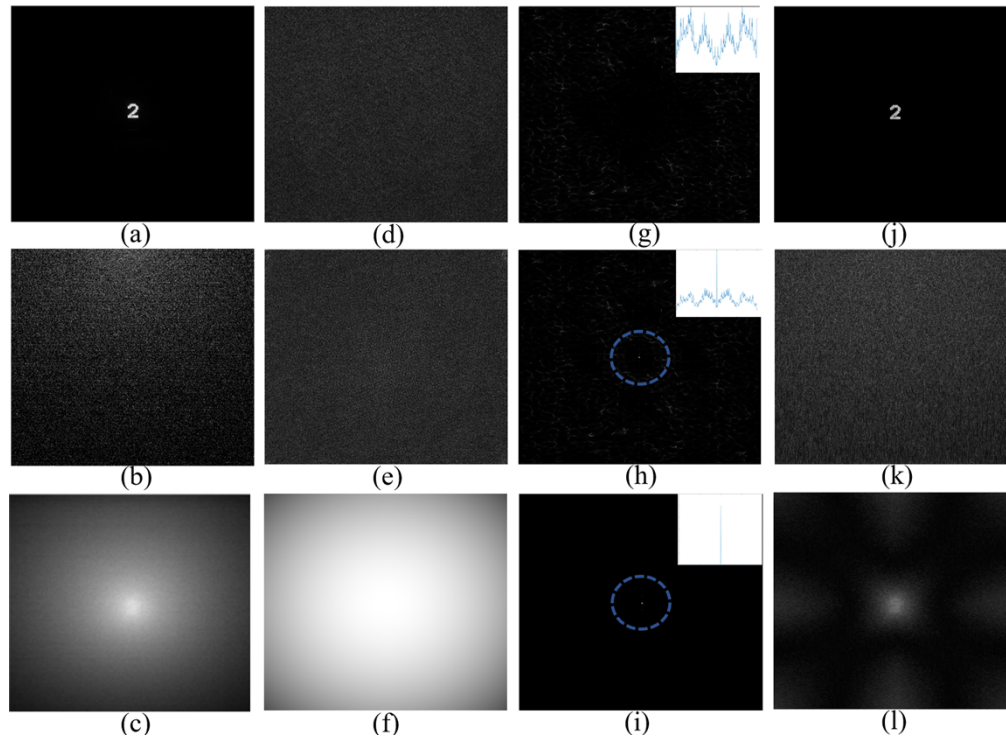


Fig. 5. The point spread function (PSF) study of optical measured PSF and calculated diffuse PSF for single perspective and light field images. (a) Ground truth image. (b) The single perspective scattering image. (c) The refocused scattering light field image. (d) The retrieved PSF from single-perspective-image-deconvolution using ground truth image (a). (e) The retrieved PSF from refocused-light-field-image-deconvolution using ground truth image (a). (f) The calculated PSF of proposed diffuse kernel. (g) The frequency spectrum of retrieved single perspective PSF shown in (b). (h) The frequency spectrum of retrieved light field image PSF (e). (i) The frequency spectrum of the PSF for light field image. (j) The reconstructed image from single perspective image using retrieved PSF (d) or from light field image using retrieved PSF (e). (k) The reconstructed image from single perspective image using calculated diffuse kernel (f). (l) The reconstructed image from refocused light field image using calculated diffuse kernel (f).

Moreover, three groups of experiments are conducted for passive-luminous targets ‘T’, ‘Tree’, and ‘Arrow’ to verify the effectiveness of the proposed method for scattering imaging in dealing with backscattering photons as shown in (a)-(c) of Fig. 6. With our measurement equipment, the optical thickness in this case is about 9, which is about 3 times visibility by using optical thickness dividing $|\log 0.05|$ [44]. As seen in Fig. 6, the images in the first column are ground truth, the images in the second column are perspective images, the images in the third column are light field images, the images in the fourth column are reconstructed images with the proposed DLIM and the images in the fifth column are light field images reconstructed by using DLIM. The backscattering photons lead to a strong background noise in DLIM-reconstructed images. Noting that even though strong background noise covers the reconstructed target signal, the targets are still visible in DLIM reconstructed images, which proves the effectiveness of utilization of forward scattering photons for passive-luminous targets. Furthermore, the DLIM gains the best

reconstruction quality with notable enhancements compared with the DLIM method. This shows the importance of removing backscattering photons to improve the SNR of the reconstructed image.

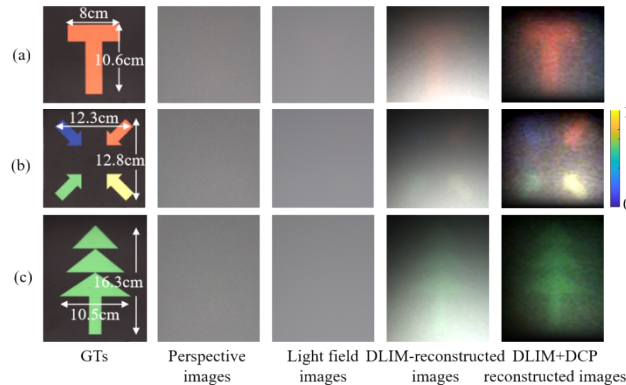


Fig. 6. Experimental results for passive-luminous scattering light field imaging. The 1st column refers to ground truths (GTs) of targets ‘T’, ‘Target’ and ‘Tree’. One of perspective images for three targets are shown in 2nd column. Light field images synthesized with perspective images are in 3rd column. The reconstructed light field images with proposed DLIM are in 4th column. The final reconstruction results with DLIM are shown in 5th column. Experiment targets contain (a) ‘T’, (b) ‘Arrow’ and (c) ‘Tree’.

To quantitatively evaluate the imaging capacity of DLIM when dealing with self and passive-luminous scattering images, the two most used image evaluation matrix, SSIM and PSNR are applied. The reference images are captured with the same light field imaging system without fog. Furthermore, the scattering imaging method under the light field imaging framework, Peplography is also implemented as a comparison of proposed methods [33]. In Peplography, all scattering photons are reduced using statistical estimation, and then the ballistic photons are accumulated using the photon counting model [31]. The input images for Peplography and DLIM are single refocused scattering light field images. Figure 7 shows the target images, Peplography reconstructed images and DLIM reconstructed images in (a)-(d). The SSIM of Peplography reconstructed images for four groups of self-luminous targets of ‘T’, ‘H’, ‘U’ and ‘2’ are 0.002, 0.015, 0.029 and 0.048, whereas the DLIM reconstructed images have SSIM values of 0.049, 0.105, 0.266 and 0.363, respectively. And the PSNRs are 9.837, 14.766, 16.950 and 18.702 for Peplography and 18.433, 19.382, 20.181 and 21.276 for DLIM, respectively. More importantly, the self-luminous targets cannot be recognized from Peplography-reconstructed images but are well observed from DLIM-reconstructed images as seen in (d) of Fig. 7. As seen in Fig. 8, the SSIM of Peplography reconstructed images for three passive-luminous targets of ‘T’, ‘Arrow’, and ‘Tree’ are 0.257, 0.255, and 0.228, whereas the DLIM reconstructed images are 0.519, 0.448, and 0.273, respectively. And the PSNRs are 12.990, 12.721, and 11.652 for Peplography and 15.701, 12.333, and 14.418 for DLIM.

As seen in Fig. 9, for passive-luminous targets, the average PSNR of Peplography and DLIM^P are 12.454 and 14.151, indicating higher 1.70 PSNR gained by DLIM^P, whereas the average SSIM are 0.247 and 0.413 for them, indicating higher 0.166 SSIM gained by DLIM^P. For self-luminous targets, the average PSNR of Peplography and DLIM^S are 15.061 and 19.818, indicating a higher 4.757 PSNR gained by DLIM^S, the average SSIM are 0.024 and 0.196, indicating higher 0.172 SSIM gained by DLIM^S.

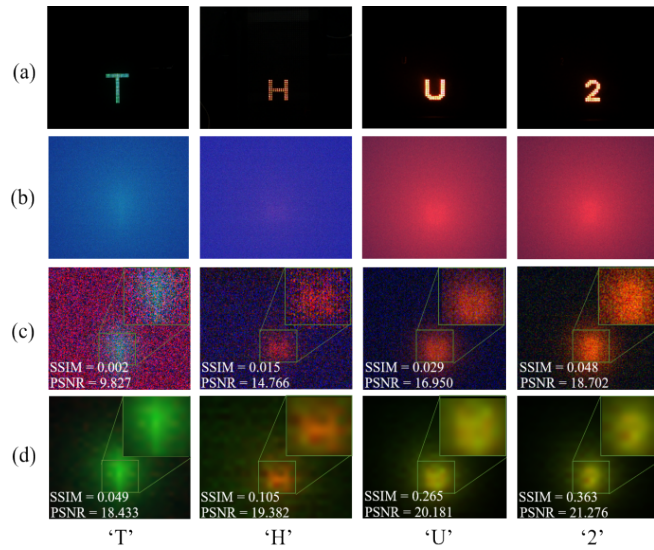


Fig. 7. Experimental comparison between Peplography and DLIM regarding self-luminous scattering light field images. (a) Ground truth. (b) Refocused scattering light field images. (c) Reconstructed images with Peplography. (d) Reconstructed images with proposed method.

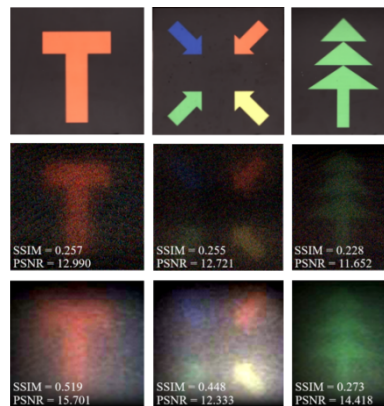


Fig. 8. Experimental comparison between Peplography and DLIM regarding passive-luminous scattering light field images.

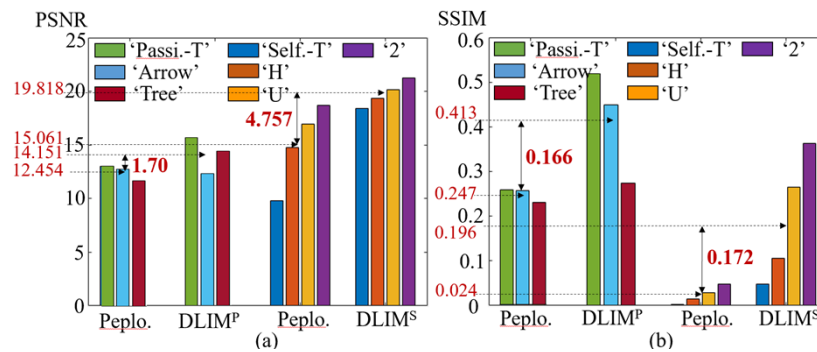


Fig. 9. Statistic analysis of reconstruction quality with respect to PSNR and SSIM for Peplography, DLIM and DLIM. (a) PSNR statistic result. (b) SSIM statistic result.

Well-known dehaze methods including image enhancement and prior-based methods are mostly ineffective when addressing these highly scattered images, which are experimentally verified as extensive experiments. [Supplement 1](#).

To study the effect of several critical model factors, such as number of perspectives of light field, anisotropic factor of scattering media and optical thickness involved in diffuse light field imaging model, the extensive experiments have been implemented to verify their influence to the imaging capacity of proposed method and the three-dimensional imaging capacity, which can be found in [Supplement 1](#).

The currently proposed model assumes that the scattering medium is homogeneous and isotropic. In practice, materials can have inhomogeneous scattering and absorption coefficients as non-uniform density distribution of volume particles. The proposed technique could potentially be extended to account for the non-uniform density of scattering media by modeling the variance under average density when performing another convolution to the diffuse kernel. In the case of serious anisotropy of media, then the diffusion approximation will be invalid. In this case, high-order P^N approximation can be used to obtain a solution for 4-D radiate light field kernel.

4. Conclusion

Optical imaging overcoming the scattering effect is challenging but significant for many fields. In this paper, a diffuse light field model is proposed to construct a novel light field imaging framework for optical imaging through highly scattering media. Moreover, by combining the classical J-M model, a complete scattering light field model can be constructed, which is a fundamental theoretical work that will feed more scattering imaging algorithms. Extensive experiments have been conducted to confirm the superior imaging capacity of the proposed methods compared to state-of-the-art scattering imaging methods for both of passive-luminous and self-luminous targets. To the best of our knowledge, this is the first physically-aware scattering light field imaging model, which might extend the light field imaging framework into scattering imaging area.

Funding. National Natural Science Foundation of China (62205178, 61991451); Shenzhen Science and Technology Project (JSGG20210802154807022); The Major Key Project of PCL (PCL2023A010).

Disclosures. The authors declare no conflicts of interest.

Data availability. Data underlying the results presented in this paper are not publicly available at this time but may be obtained from the authors upon reasonable request.

Supplemental document. See [Supplement 1](#) for supporting content.

References

1. B. L. McGlamery, "A computer model for underwater camera systems," *Proc. SPIE* **0208**, 221–231 (1980).
2. J. S. Jaffe, "Computer modeling and the design of optimal underwater imaging systems," *IEEE J. Oceanic Eng.* **15**(2), 101–111 (1990).
3. C. Liu and M. Wang, "Removal of water scattering," *2010 2nd international conference on computer engineering and technology* (2010).
4. G. Narasimhan, K. Srinivasa, and Nayar Shree, "Chromatic framework for vision in bad weather," *IEEE Conf. Comput. Vis. Pattern Recognit.* 589–605 (2000).
5. K. He, J. Sun, and X. Tang, "Single image haze removal using dark channel prior," *IEEE Trans. Pattern Anal. Mach. Intell.* **33**(12), 2341–2353 (2011).
6. Y. Yan, W. Ren, Y. Guo, *et al.*, "Image deblurring via extreme channels prior," In *Proceedings of the IEEE Conf. Comput. Vis. Pattern Recognit.*, 4003–4011 (2017).
7. D. Berman and S. Avidan, "Non-local image dehazing," *IEEE Conf. Comput. Vis. Pattern Recognit.*, 1674–1682, (2016).
8. D. Berman, T. Treibitz, and S. Avidan, "Single image dehazing using haze-lines," *IEEE Trans. Pattern Anal. Mach. Intell.* **42**(3), 720–734 (2020).
9. D. Berman, D. Levy, S. Avidan, *et al.*, "Underwater single image color restoration using haze-lines and a new quantitative dataset," *IEEE Trans. Pattern Anal. Mach. Intell.* **43**(8), 2822–2837 (2021).
10. Q. Zhu, J. Mai, and L. Shao, "A fast single image haze removal algorithm using color attenuation prior," *IEEE Trans. Image Process* **24**(11), 3522–3533 (2015).

11. M. Ju, C. Ding, Y. J. Guo, *et al.*, "IDGCP: Image Dehazing Based on Gamma Correction Prior," *IEEE Trans. Image Process* **29**(15), 3104–3118 (2020).
12. C. Ancuti, C. O. Ancuti, T. Haber, *et al.*, "Enhancing underwater images and videos by fusion," *IEEE Conf. Comput. Vis. Pattern Recognit.*, 81–88 (2012).
13. C. O. Ancuti and C. Ancuti, "Single Image Dehazing by Multi-Scale Fusion," *IEEE Trans. Image Process* **22**(8), 3271–3282 (2013).
14. G. Hines, Z. U. Rahman, D. Jobson, *et al.*, "Single-scale retinex using digital signal processors," In *Global signal processing conference, No. Paper 1324*, (2005).
15. Z. Rahman, J. Jobson Daniel, and A. Woodell Glenn, "Multi-scale retinex for color image enhancement," *Proceedings of 3rd IEEE international conference on image processing*, 3. IEEE, 1996.
16. J. Xie, G. Hou, G. Wang, *et al.*, "A variational framework for underwater image dehazing and deblurring," *IEEE Trans. Circuits Syst. Video Technol* **32**(6), 3514–3526 (2022).
17. G. Hou, N. Li, P. Zhuang, *et al.*, "Non-uniform illumination underwater image restoration via illumination channel sparsity prior," *IEEE Trans. Circuits Syst. Video Technol* **34**(2), 799–814 (2024).
18. W. Zhang, L. Zhou, P. Zhuang, *et al.*, "Underwater image enhancement via weighted wavelet visual perception fusion," *IEEE Trans. Circuits Syst. Video Technol* **34**(4), 2469–2483 (2024).
19. G. Satat, M. Tancik, and R. Raskar, "Towards photography through realistic fog," In *2018 IEEE International Conference on Computational Photography (ICCP)*, 1–10 (2018).
20. J. Y. Chiang and Y. C. Chen, "Underwater image enhancement by wavelength compensation and dehazing," *IEEE Trans. Image Process.* **21**(4), 1756–1769 (2012).
21. O. Katz, P. Heidmann, M. Fink, *et al.*, "Non-invasive single-shot imaging through scattering layers and around corners via speckle correlations," *Nat. Photonics* **8**(10), 784–790 (2014).
22. X. Y. Wang, X. Jin, J. Q. Li, *et al.*, "Prior-information-free single-shot scattering imaging beyond the memory effect," *Opt. Lett.* **44**(6), 1423–1426 (2019).
23. S. M. Popoff, G. Lerosey, R. Carminati, *et al.*, "Measuring the transmission matrix in optics: an approach to the study and control of light propagation in disordered media," *Phys. Rev. Lett.* **104**(10), 100601 (2010).
24. S. Popoff, G. Lerosey, M. Fink, *et al.*, "Image transmission through an opaque material," *Nat. Commun.* **1**(1), 81 (2010).
25. Z. Yaqoob, D. Psaltis, M. S. Feld, *et al.*, "Optical phase conjugation for turbidity suppression in biological samples," *Nat. Photonics* **2**(2), 110–115 (2008).
26. Y. Liu, C. Ma, Y. Shen, *et al.*, "Focusing light inside dynamic scattering media with millisecond digital optical phase conjugation," *Optica* **4**(2), 280–288 (2017).
27. I. M. Vellekoop and A. P. Mosk, "Focusing coherent light through opaque strongly scattering media," *Opt. Lett.* **32**(16), 2309–2311 (2007).
28. X. Zhang and P. Kner, "Binary wavefront optimization using a genetic algorithm," *J. Opt.* **16**(12), 125704 (2014).
29. S. Komatsu, A. Markman, and B. Javidi, "Optical sensing and detection in turbid water using multidimensional integral imaging," *Opt. Lett.* **43**(14), 3261–3264 (2018).
30. I. Moon and B. Javidi, "Three-dimensional visualization of objects in scattering medium by use of computational integral imaging," *Opt. Express* **16**(17), 13080–13089 (2008).
31. B. Tavakoli, B. Javidi, and E. Watson, "Three dimensional visualization by photon counting computational integral imaging," *Opt. Express* **16**(7), 4426–4436 (2008).
32. M. Cho and B. Javidi, "Three-dimensional visualization of objects in turbid water using integral imaging," *J. Display Technol.* **6**(10), 544–547 (2010).
33. M. Cho and B. Javidi, "Peplography—a passive 3D photon counting imaging through scattering media," *Opt. Lett.* **41**(22), 5401–5404 (2016).
34. M. Martínez-Corral and B. Javidi, "Fundamentals of 3D imaging and displays: A tutorial on integral imaging, Lightfield, and plenoptic systems," *Adv. Opt. Photonics* **10**(3), 512–566 (2018).
35. B. Javidi, A. Carnicer, J. Arai, *et al.*, "Roadmap on 3D integral imaging: sensing, processing, and display," *Opt. Express* **28**(22), 32266–32293 (2020).
36. K. Usmani, T. O'Connor, P. Wani, *et al.*, "3D object detection through fog and occlusion: passive integral imaging vs active (LiDAR) sensing," *Opt. Express* **31**(1), 479–491 (2023).
37. G. Krishnan, R. Joshi, T. O'Connor, *et al.*, "Optical signal detection in turbid water using multidimensional integral imaging with deep learning," *Opt. Express* **29**(22), 35691–35701 (2021).
38. A. J. Welch and J. C. Martin Gemert, "Optical-Thermal Response of Laser-Irradiated Tissue," Chap.6, Springer (1995).
39. P. Adam, C. Jeremy, and R. Simon, "Recent advances in diffuse optical imaging," *Phys. Med. Biol.* **50**(4), R1 (2005).
40. J. Bertolotti and O. Katz, "Imaging in complex media," *Nat. Phys.* **18**(9), 1008–1017 (2022).
41. S. L. Jacques and W. P. Brian, "Tutorial on diffuse light transport," *J. Biomed. Opt.* **13**(4), 041302 (2008).
42. R. C. Haskell, L. O. Svaasand, T.-T. Tsay, *et al.*, "Boundary conditions for the diffusion equation in radiative transfer," *J. Opt. Soc. Am. A* **11**(10), 2727–2741 (1994).
43. N. Ren, "Fourier slice photography," *ACM Siggraph* **24**(3), 735–744 (2005).
44. S. G. Narasimhan, "Models and algorithms for vision through the atmosphere," Chap.6, Columbia University (2004).
45. Z. Y. Zhang, "A flexible new technique for camera calibration," *IEEE Trans. Pattern Anal. Machine Intell.* **22**(11), 1330–1334 (2000).